Atmospheric
Measurement
Techniques

How bias correction goes wrong: measurement of X_{CO_2} affected by erroneous surface pressure estimates

Matthäus Kiel[1], **Christopher W. O'Dell**[4], **Brendan Fisher**[3], **Annmarie Eldering**[3], **Ray Nassar**[5], **Cameron G. MacDonald**[6], and **Paul O. Wennberg**[1,2]

[1]Division of Geological and Planetary Sciences, California Institute of Technology, Pasadena, CA, USA
[2]Division of Engineering and Applied Sciences, California Institute of Technology, Pasadena, CA, USA
[3]Jet Propulsion Laboratory, California Institute of Technology, Pasadena, CA, USA
[4]Colorado State University, Fort Collins, CO, USA
[5]Climate Research Division, Environment and Climate Change Canada, Toronto, ON, Canada
[6]Department of Physics and Astronomy, University of Waterloo, Waterloo, ON, Canada

Correspondence: Matthäus Kiel (mkiel@caltech.edu)

Abstract. All measurements of X_{CO_2} from space have systematic errors. To reduce a large fraction of these errors, a bias correction is applied to X_{CO_2} retrieved from GOSAT and OCO-2 spectra using the ACOS retrieval algorithm. The bias correction uses, among other parameters, the surface pressure difference between the retrieval and the meteorological reanalysis. Relative errors in the surface pressure estimates, however, propagate nearly 1 : 1 into relative errors in bias-corrected X_{CO_2}. For OCO-2, small errors in the knowledge of the pointing of the observatory (up to ~ 130 arcsec) introduce a bias in X_{CO_2} in regions with rough topography. Erroneous surface pressure estimates are also caused by a coding error in ACOS version 8, sampling meteorological analyses at wrong times (up to 3 h after the overpass time). Here, we derive new geolocations for OCO-2's eight footprints and show how using improved knowledge of surface pressure estimates in the bias correction reduces errors in OCO-2's v9 X_{CO_2} data.

1 Introduction

Atmospheric carbon dioxide (CO_2) is currently being measured from space by, among other instruments, NASA's Orbiting Carbon Observatory 2 (OCO-2) and JAXA's Greenhouse gases Observing SATellite (GOSAT). Accurate and precise measurements of atmospheric CO_2 can identify and

quantify its sources and sinks and, more generally, improve our understanding of biosphere–atmosphere fluxes. To do so, these measurements must be sufficiently accurate and precise to properly capture the small ($< 1\%$) spatial and temporal gradients of CO_2. OCO-2 and GOSAT X_{CO_2} data have been widely used in studies to characterize fluxes from different sources, e.g., emissions from power plants (Nassar et al., 2017) or fires in Indonesia (Heymann et al., 2017). Other recent studies analyzed flux anomalies during El Niño periods (Liu et al., 2017).

OCO-2 and GOSAT share a common observational approach: solar reflectance spectra centered around 1.6 and 2.0 µm are used to determine the CO_2 optical depth. The O_2 optical depth is observed in the so-called "A band" centered around 0.76 µm. The column-averaged dry air mole fraction of CO_2 (X_{CO_2}) is determined by combining the information from these three spectral regions. The A band is used to determine the amount of dry air along the O_2 optical path from the sun to the spectrometer (air mass). The two CO_2 bands provide a measure of how many CO_2 molecules are in the similar paths. X_{CO_2} is the ratio of CO_2 to the dry surface pressure. Any error that does not affect both the CO_2 measurement and dry surface pressure in the same way is expected to propagate into X_{CO_2}. A fundamental challenge for the retrieval is that photons are scattered in the atmosphere, and the efficiency of the scattering – primarily by clouds and aerosols – depends on wavelength. The wavelength-dependent scat-

tering is, in turn, estimated by the retrieval algorithm using information from both the O_2 spectra and the relative CO_2 optical depths determined from the two different CO_2 bands.

Early analysis of X_{CO_2} from the initial GOSAT spectra had global and regional systematic errors. Wunch et al. (2011b) demonstrated, however, that a large fraction of the error in X_{CO_2} was correlated with retrieved components of the state vector in the retrieval algorithm. In particular, difference between the retrieval of surface pressure and that from the meteorological reanalysis was shown to correlate with error of similar magnitude in X_{CO_2} (e.g., when the surface pressure retrieval was $\sim 1\%$ too large, the retrieved X_{CO_2} was $\sim 1\%$ too small). There are several reasons why surface pressure is not accurately retrieved from the spectra. First, errors in the knowledge of the spectroscopy of oxygen can produce spurious air mass dependencies and can affect the pressure retrieval (e.g., Yang et al., 2005; Wunch et al., 2011a). Second, the algorithm is not adequately able to distinguish pathlength errors due to scattering from those due to surface pressure variation. For example, overestimates of the amount of aerosol near the surface (which shortens the path) can be compensated for by an overestimate of surface pressure. Because in the retrieval aerosols are generally assumed to scatter less efficiently at longer wavelengths, error in retrieved pathlength maps differently into O_2 and CO_2, resulting in a bias in X_{CO_2}. Pathlength errors also largely depend on surface albedo. For example, if the surface albedo is high, multiple reflections between the surface and the aerosol layer are efficient and lengthen the path. Moreover, the spectral variation of surface albedo and aerosol optical properties also change the radiative transfer between the A band and CO_2 bands. For example, differences in the absorption optical thickness structure between the three bands induce band-dependent height sensitivities to different types of aerosols in the retrieval.

Several retrieval codes that have been used to analyze GOSAT and OCO-2 spectra treat this problem differently. For example, the RemoTeC algorithm does not retrieve the surface pressure from the spectra. It uses the surface pressure from the meteorological reanalysis (Butz et al., 2011; Wu et al., 2018). Others, such as the University of Leicester Full Physics algorithm (UoL-FP) first normalizes the retrieved X_{CO_2} by the ratio of the retrieved surface pressure from the spectra and the surface pressure from the meteorological reanalysis. Then it uses the difference between the retrieved surface pressure and that from the meteorological reanalysis to "bias correct" the X_{CO_2} product (Cogan et al., 2012). To date, all versions of the Atmospheric Carbon Observations from Space (ACOS) retrieval algorithm (O'Dell et al., 2012, 2018; Crisp et al., 2012), used for both OCO-2 and GOSAT spectra, have also used the surface pressure difference between the retrieval and that diagnosed from the meteorological reanalysis to bias correct the X_{CO_2} product. This bias correction demonstrably improves the data set (Wunch et al., 2011b, 2017b; O'Dell et al., 2018). It also, however, places

new demands on the accuracy of the meteorological analysis – demands that had not been considered at the time the OCO-2 mission was conceived. Error in the assumed pressure from the meteorological reanalyses at the field of view of the spectrometers will propagate nearly $1:1$ into bias-corrected X_{CO_2}. Over land, for example, small errors in the knowledge of the pointing of the observatory can yield significant errors in estimates of surface pressure in regions with rough topography. This is illustrated in Wunch et al. (2017b), in which X_{CO_2} variations near Lauder, New Zealand, showed strong sensitivity to (different) estimates of the pointing of OCO-2, introducing an apparent topography-related bias in the data. Finally, due to atmospheric tides, the estimate of the surface pressure is sensitive to when the meteorological reanalysis is sampled. Given the precision we need to achieve in X_{CO_2} measurements, seemly insignificant issues can not necessarily be ignored. For example, the mean canopy height of the Amazon rain forest is ~ 25 m (Benson et al., 2016) and might vary temporally due to fires or deforestation. Furthermore, the usual tidal range in the open ocean is ~ 0.5 m, but coastal tidal ranges can reach up to 12 m (NOAA, 2018). At sea level, altitude variations of ~ 8 m correspond to changes in surface pressure of ~ 1 hPa. This might introduce errors in X_{CO_2} on the order of ~ 0.4 ppm.

In this analysis, we address two issues with the OCO-2 v8 estimate of surface pressure: erroneous surface pressure values from the meteorological reanalysis due to small miss-specifications of the geolocations of OCO-2's eight footprints in the instrument-to-spacecraft pointing offsets and erroneous surface pressure estimates due to sampling the meteorological reanalysis at incorrect times. We illustrate how, using improved knowledge of the surface pressure, we can improve the bias correction and reduce errors in X_{CO_2}. The resulting hybrid product which uses version 8 (v8) retrieval results with a revised bias correction using updated surface pressure estimates is labeled as version 9 (v9). This paper is structured as follows: Sect. 2 describes the impact of erroneous surface pressure estimates in the bias correction on X_{CO_2} estimates. New footprint geolocations for OCO-2 are derived in Sect. 3. Section 4 introduces the revised parametric bias correction in v9 and discusses changes in the v9 filtration scheme. Section 5 gives a brief evaluation of the OCO-2 v9 data product and illustrates changes and improvements of v9 over v8 X_{CO_2} on regional and global scales.

2   Biases in OCO-2 X_{CO_2} due to erroneous surface pressure estimates

OCO-2 v8 X_{CO_2} estimates are derived using the ACOS retrieval algorithm. The algorithm uses optimal estimation to solve for parameters of the state vector to obtain the best match to spectra recorded in OCO-2's three spectral bands. The state vector includes, among other parameters, the surface pressure which is primarily derived from information

retrieved from the O_2 A band. The prior surface pressure is taken from the GEOS-5 Forward Processing for Instrument Teams Atmospheric Data Assimilation System (GEOS5-FP-IT; Suarez et al., 2008; Lucchesi, 2013) and is sampled at the geolocation of each OCO-2 sounding. Surface pressure and prior surface pressure are used in the bias correction of X_{CO_2}. The OCO-2 bias correction addresses three types of biases: footprint-dependent biases, parameter-dependent biases, and a global scaling of X_{CO_2} to the World Meteorological Organization (WMO) trace-gas standard scale using comparisons to the Total Carbon Column Observing Network (TCCON; Wunch et al., 2011a). An overview of the three different bias correction terms is given in Mandrake et al. (2015), Wunch et al. (2017b), and O'Dell et al. (2018).

Biases in OCO-2 X_{CO_2} due to erroneous surface pressure estimates were initially illustrated in OCO-2 observations over Lauder, New Zealand (Fig. 10 in Wunch et al., 2017b). The Lauder TCCON site is situated in a remote area with no urban sources of X_{CO_2} nearby (Pollard et al., 2017). The area is dominated by rolling hills, with mountain ridges spanning from southwest to northeast, almost perpendicular to the ground track of the observatory (southeast to northwest). The terrain changes up to ± 200 m in altitude over small distances (see Fig. 1a). Figure 1b shows X_{CO_2} enhancements retrieved by the ACOS algorithm (v8) over Lauder for a target observation on 17 February 2015. No bias correction is applied here. X_{CO_2} estimates are uniformly distributed over the observed scene with a mean value of 393.58 ppm and a standard deviation of 0.92 ppm. Figure 1c shows OCO-2 X_{CO_2} estimates after the v8 bias correction is applied. The bias correction changes the mean value to 395.95 ppm and increases the standard deviation to 1.35 ppm. Bias-corrected X_{CO_2} enhancements vary up to ± 3 ppm over the observed scene. The bias is spatially correlated with the underlying topography, more precisely, with the topographic slopes. The observed bias is introduced by erroneous values of the prior surface pressure in the dP term (the difference between the retrieved surface pressure and the prior surface pressure) in the parametric bias correction. The parametric bias correction accounts for spurious variability in X_{CO_2} which correlates with retrieval parameters like albedo, retrieval aerosol quantities, or surface pressure. A multivariate regression is performed between spurious X_{CO_2} variability and the parameters that account for the largest variance in the data to correct for these errors (Wunch et al., 2011b; Mandrake et al., 2015; O'Dell et al., 2018). The erroneous values of the prior surface pressure are caused by small misspecifications in the geolocations of OCO-2's eight footprints in the specified instrument-to-spacecraft pointing. As stated previously, at sea level, a surface pressure difference of 1 hPa corresponds to an altitude difference of ~ 8 m. Therefore, in areas like Lauder with steep topography, misspecifications in the pointing of the observatory of a few arcseconds can cause the prior surface pressure to be substantially different from the retrieved surface pressure. This introduces errors in bias-corrected X_{CO_2},
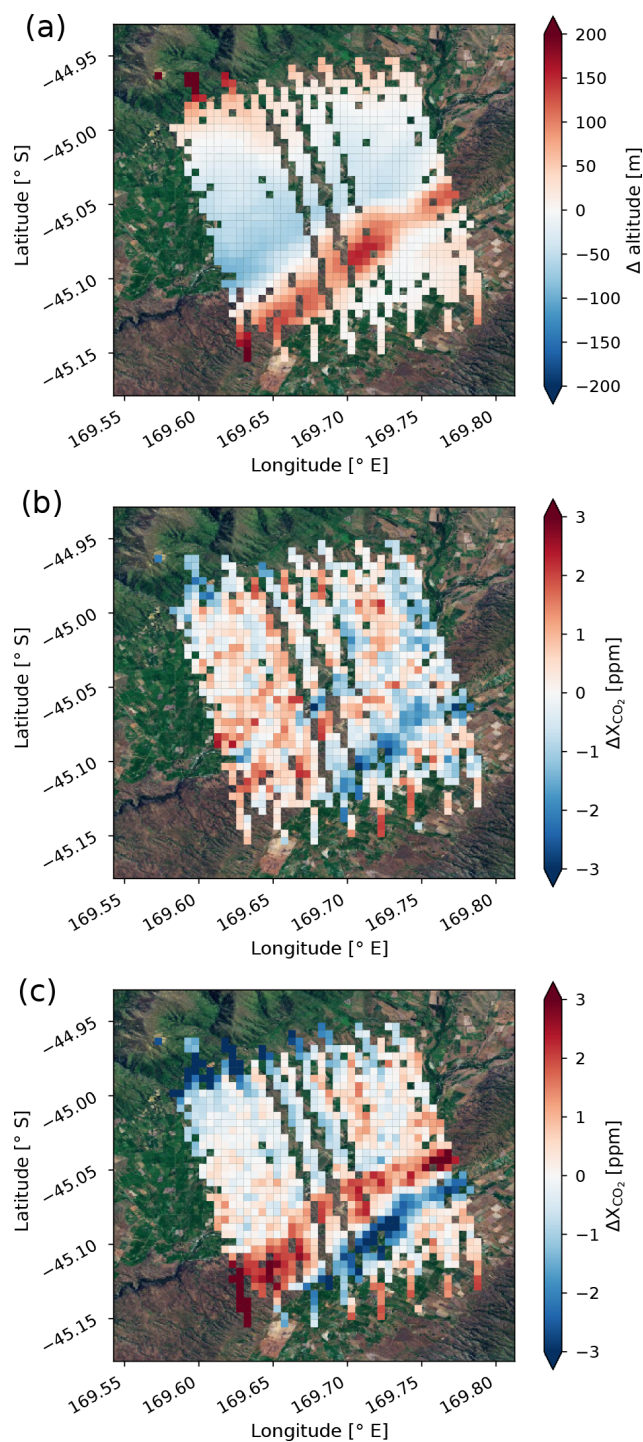

Figure 1. OCO-2 target mode observation over Lauder, New Zealand, on 17 February 2015. Panel **(a)** shows Δ altitude (defined as the sounding altitude minus the median altitude of all soundings in the given latitude and longitude limits). Panels **(b)** and **(c)** show the variation of raw and bias-corrected OCO-2 v8 ΔX_{CO_2} (defined in the same way as Δ altitude) after applying the v8 filters. Individual soundings are aggregated into $0.005° \times 0.005°$ latitude–longitude square grids.
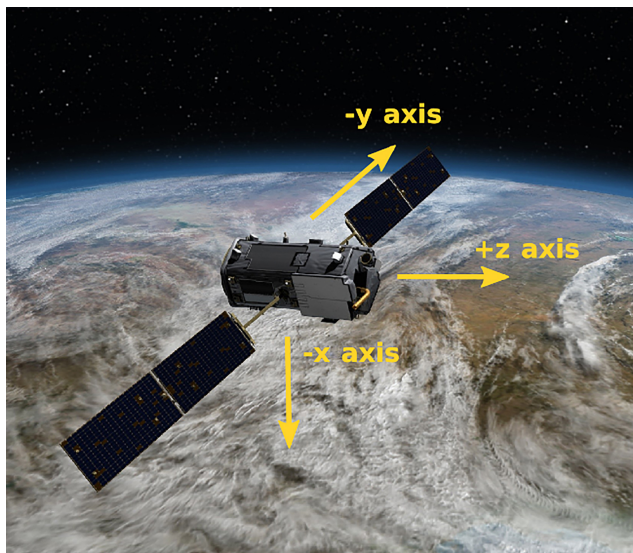
Figure 2. Illustration of the OCO-2 spacecraft body axes.

typically observed on local scales in areas with highly varying topography.

Another source for erroneous surface pressure estimates in v8 is caused by a temporal sampling error of the surface pressure estimate from the meteorological reanalysis. The prior surface pressure is taken from the GEOS5-FP-IT 3-hourly output. A coding error in the meteorological sampling algorithm caused for some soundings the surface pressure estimate to be sampled as much as 3 h after the overpass time. This mostly affected soundings of orbits whose first and last soundings fully lie between synoptic GEOS5-FP-IT's 3-hourly outputs (00:00, 03:00, etc.); the soundings in such an orbit would be erroneously sampled at the upper bounding synoptic time for that orbit. For example, for an orbit whose soundings lie fully between 06:00 and 09:00 UTC, the OCO-2 meteorological sampling algorithm erroneously samples the GEOS5-FP-IT surface pressure field at 09:00 UTC for each sounding in that orbit. On average, this introduced a mean prior surface pressure error of about $+0.5$ hPa for affected soundings. In some cases, however, the prior surface pressure error reached up to ± 20 hPa for individual soundings. The sampling error also affects temperature and water vapor. Soundings over land are affected more than over ocean since diurnal surface heating tends to be stronger over land and because the surface pressure bias correction term over land is nearly 50 % larger than over water. While the sampling error of the prior surface pressure is easy to correct for via the bias correction by fixing the coding error and rerunning the meteorological sampling algorithm, erroneous surface pressure estimates caused by misspecifications in the instrument pointing offsets need greater attention.
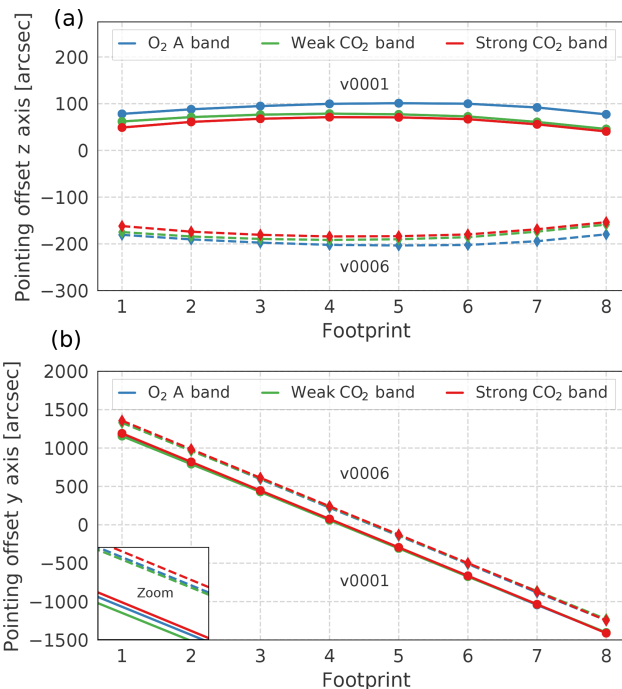

Figure 3. OCO-2 pointing offsets for each footprint and spectral band for the z axis (**a**) and y axis (**b**) derived from the pre-launch (v0001) and on-orbit (v0006) analyses.

3 Evaluation of OCO-2's footprint geolocations

The core of the OCO-2 instrument is a three-channel grating spectrometer that records spectra of reflected sunlight in the O_2 A band (0.76 µm), the weak CO_2 band (1.61 µm), and the strong CO_2 band (2.06 µm). The incoming light is guided through a common optics assembly, but the light is sampled and focused sequentially and independently onto three spectrometer slits, each 3 mm long and 28 µm wide (Haring et al., 2004; Crisp et al., 2017). These long, narrow slits are aligned to produce nominally co-boresighted fields of view. After passing the slit and being spectrally dispersed, the light is focused on a two-dimensional focal plane array (FPA) with eight independent readouts along the slits – the so-called footprints. Spectra for the three spectral bands and each footprint are recorded simultaneously.

To obtain the best estimate for the geolocation of the eight footprints, the following must be known: (1) the location of the spacecraft along the orbit track, (2) the pointing of the instrument boresight relative to a local coordinate system, and (3) the relative pointing of the fields of view (FOV) of the eight footprints in the three spectrometers. A Global Positioning System (GPS) sensor provides the location of the observatory along its orbit track. The on-board star tracker determines the orientation of the observatory relative to fixed stars. The relative alignment of the eight footprints is characterized with respect to the spacecraft body axes. The spatial FOV, defined along the long axis of the slit by the eight foot-

prints, is aligned parallel with the spacecraft y axis. The boresight of the spectrometer points down the x axis. The spacecraft z axis points across the narrow axis of the spectrometer slit, perpendicular to the y axis (see Fig. 2). For nadir and glint measurements, the z axis is rotated around the x axis so it is oriented 30° (clockwise from above) from the principal plane (i.e., the plane that includes the sun, the surface target, and the instrument aperture). To maintain this viewing geometry, the spacecraft slowly rotates counterclockwise (from above) around the x axis as it travels from the southern terminator, across the sub-solar latitude, to the northern terminator. South of a latitude that is $\sim 30°$ north of the sub-solar latitude, footprint 1 (FP 1) is to the west of footprint 8 (FP 8). North of this latitude, FP 1 is east of FP 8. For target mode observations, the z axis is always pointed along the spacecraft orbit track, so that FP 1 is always to the west of FP 8. Pre-launch instrument ground tests were performed to characterize the spatial FOV of each footprint, and correction factors – the so-called pointing offsets – have been derived and integrated into the geometric calibration algorithm (v0001 configuration; see Fig. 3). The pointing offsets are on the order of hundreds of arcseconds. A change in the pointing offsets of, for example, 25 arcsec corresponds to a shift of the instrument FOV of $\sim 80\,\mathrm{m}$ at nadir. During the OCO-2 in-orbit checkout (IOC) period in 2014, lunar measurements were performed, and in combination with data from coastal crossings the alignment of the three spectrometer slits was tested. The alignment of the instrument angular footprints in the coordinate system defined by the star tracker was within mission requirements (< 720 arcsec). Updated pointing offsets were integrated into the geometric calibration algorithm in November 2014 (v0006 configuration; see Fig. 3). The findings in the previous section, however, indicate that a reevaluation of the pointing vector correction factors is desirable.

3.1 Methodology

The analysis of the IOC lunar data exposed some deficiencies of its usage in elaborating footprint geolocations. Lunar data are typically taken in so-called single pixel mode when each pixel of the array is read out individually. This is in contrast to normal operations where 20 spatial pixel samples are co-added to form each footprint. In addition, the moon only illuminates a fraction of the FPA. Furthermore, defocus compromises the analysis of the strong CO_2 band results, and the moon only provides positive constraints for the z axis.

To overcome the aforementioned limitations for the v0006 configuration, the IOC lunar data results were used to constrain the pointing vector for FP 6 and 7, whereas for the other FPs the ground test results were used. Here, we follow a different approach to derive new pointing offsets. We shift from estimating geolocations with lunar images, which are strictly geometric measurements, to optimizing footprint geolocations with retrieval variables. We utilize the ACOS

Level 2 Full Physics (L2FP) algorithm and its associated pre-screeners, the A-band Preprocessor (ABP) and the IMAP-DOAS Preprocessor (IDP) to estimate footprint geolocations. The ABP performs a fast retrieval of surface pressure using the O_2 A band and assumes that no clouds or aerosols are present. The IDP performs clear-sky fits to the weak and strong CO_2 bands to derive CO_2 columns (Taylor et al., 2016). Using the preprocessors instead of the L2FP algorithm saves computational effort and allows us to study pointing offsets for each spectral band individually. The footprint geolocations for the O_2 A band are derived by minimizing the variation in the difference between the surface pressure retrieved from the ABP and the meteorological analysis ($\mathrm{d}P_{\mathrm{ABP}}$). The location of the CO_2 band footprints is determined by minimizing the variation in the CO_2 columns divided by the dry air column determined from the meteorological analysis ($X_{CO_2,\mathrm{met}}$). These two metrics are systematically explored for a set of different pointing offsets. The geolocations that provide the smallest standard deviation over a given scene for $\mathrm{d}P_{\mathrm{ABP}}$ are good estimates for the location of the O_2 A band. The same holds for the standard deviation of $X_{CO_2,\mathrm{met}}$ regarding the weak and strong CO_2 band. The assumption here is that there are no significant variations in X_{CO_2} over the field of analysis. This may not be true in regions with large heterogeneous sources (e.g., urban areas) or sinks (vegetated areas) of CO_2. It is only true for areas with a clean X_{CO_2} background. Therefore, in our analysis we focus on remote desert-like mountainous areas to study pointing offsets.

3.2 Training data set

We identify two desert areas in the Northern and Southern Hemisphere with topographic relief and frequent clear-sky conditions during nadir and glint observations to derive new footprint geolocations: a remote area in the Death Valley National Park, CA, USA, and an area in the Atacama Desert, Chile. The Death Valley National Park area ranges from 35 to 37° N and from 118 to 115° W. The area in the Atacama Desert ranges from 18 to 19° S and from 69.8 to 69.25° W. Both areas are far from anthropogenic CO_2 sources. A topography-related bias in v8 X_{CO_2} is apparent in both areas (see Fig. 4). Observations over the Death Valley National Park include ~ 1800 soundings from September 2014 to September 2017. Observations over the Atacama Desert include ~ 1000 soundings from September 2014 to October 2017. All these soundings are aggregated into $0.02° \times 0.02°$ latitude–longitude grids. To account for the secular increase and seasonal cycle in CO_2 and different air mass values for different overpasses for each orbit, we normalize all $X_{CO_2,\mathrm{met}}$ soundings by the orbital mean. The orbital mean is calculated by taking into account all soundings of a particular orbit that are within the latitude and longitude limits of the analyzed scene. The standard deviation of $\mathrm{d}P_{\mathrm{ABP}}$ and $X_{CO_2,\mathrm{met}}$ is calculated by taking into account
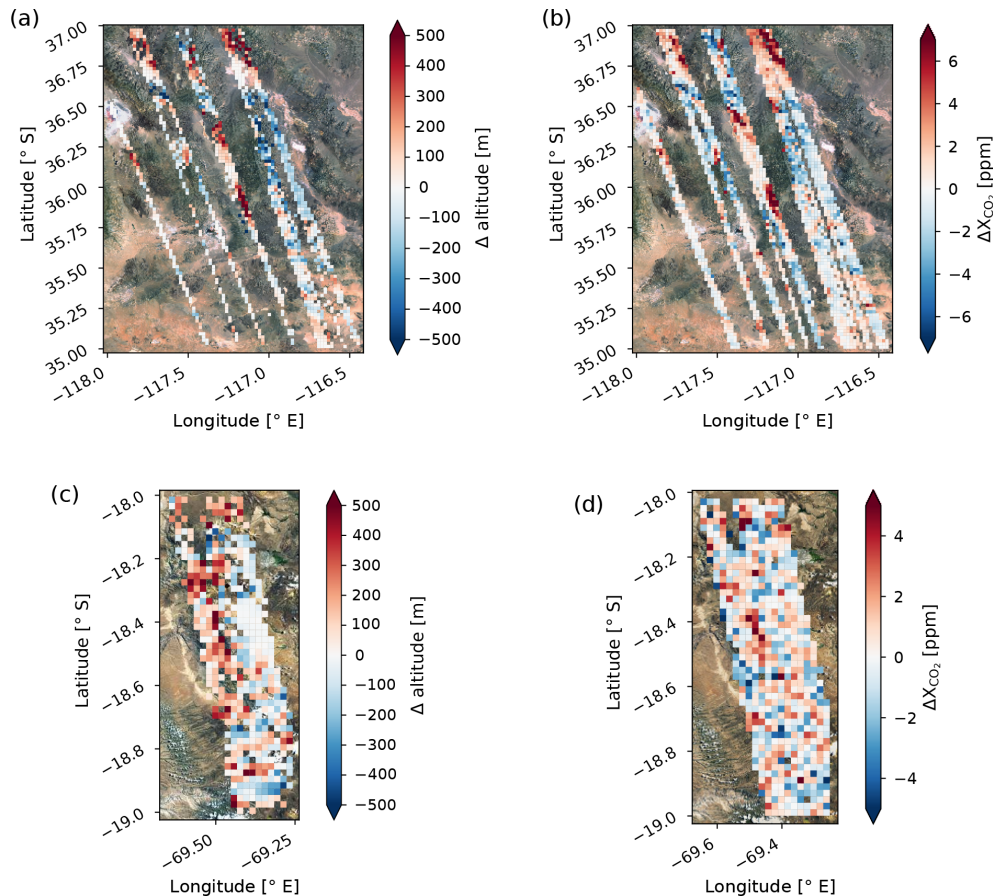
Figure 4. Change in altitude **(a, c)** over the two selected areas in the Death Valley National Park **(a, b)** and Atacama Desert **(c, d)**. The change in altitude is determined from two $0.02° \times 0.02°$ latitude–longitude grid squares in the NE direction in the Northern Hemisphere and the SE direction in the Southern Hemisphere; hence the figures have fewer values than for ΔX_{CO_2} **(b, d)**. Steep topography with total altitude changes of up to 1000 m is observed in both areas. A topography-related bias in ΔX_{CO_2} derived from the ACOS L2FP retrieval is apparent in both regions. Individual observations are aggregated into $0.02° \times 0.02°$ latitude–longitude grid squares.

all grid squares in the analyzed latitude and longitude limits. Analyzing data from both hemispheres allows us to check for possible errors introduced by the reversed orientation of the z and y axis in the Northern and Southern Hemisphere in our pointing offset derivation (e.g., errors introduced by a timing error).

We run the ABP and IDP for a set of different pointing offsets for which the relative footprint positions of the v0006 configuration are preserved. If not otherwise stated, in the following we refer to the pointing offset of FP 4 of the O_2 A band when we refer to pointing offset values. For example, if the pointing offset of FP 4 of the O_2 A band is shifted by +25 arcsec along the y axis, then all other footprint geolocations are also shifted in the same direction by +25 arcsec along the y axis (even though their absolute positions differ from the FP 4 O_2 A-band position). The same holds for the z axis. For the y axis, we run both algorithms for four different pointing offsets ranging from 175 to 250 arcsec in 25 arcsec steps. For each of these shifts, we also run a set of differ-

ent offsets for the z axis, ranging from −250 to +100 arcsec, also in 25 arcsec steps. This leads to a total of 60 different geolocation configurations.

3.3 Results

Figure 5 shows the standard deviation of dP_{ABP} and $X_{CO_2,met}$ for FP 4 for all 60 geolocation configurations for the Death Valley National Park. The observed metrics are less sensitive to changes along the footprint axis than along the z axis. Differences in the standard deviation between neighboring pointing offsets are small, typically < 0.5 hPa for the O_2 A band and < 0.2 ppm for the two CO_2 bands. This holds for all footprints in the three spectral bands. For example, for FP 2 to 7, the standard deviation of dP_{ABP} is minimized for a pointing offset of 225 arcsec along the footprint axis. A pointing offset of 200 arcsec minimizes the standard deviation of FP 1 and 8. Similar results are derived for the Atacama Desert (not shown here). In general, a pointing offset of 225 arcsec along the footprint axis minimizes the stan-

Table 1. OCO-2 v9 instrument-to-spacecraft pointing offsets for each spectral band along the y axis and z axis relative to the central boresight of the telescope in units of arcsec.

		FP1	FP2	FP3	FP4	FP5	FP6	FP7	FP8
y axis	O_2 A band	1339.5	972.4	597.2	225.0	−140.6	−508.1	−879.6	−1241.6
	weak CO_2 band	1331.0	966.2	604.7	235.9	−131.5	−499.4	−860.8	−1226.4
	strong CO_2 band	1359.1	987.3	614.7	244.0	−125.9	−496.0	−867.1	−1242.7
z axis	O_2 A band	−96.4	−109.0	−117.8	−122.8	−124.1	−121.6	−115.3	−105.2
	weak CO_2 band	−58.0	−62.9	−65.7	−66.4	−65.0	−61.4	−55.7	−47.9
	strong CO_2 band	−55.2	−57.9	−58.4	−56.6	−52.6	−46.4	−37.9	−27.2

dard deviation of dP_{ABP} and $X_{CO_2,met}$ for the majority of the footprints. This offset value is nearly identical to the v0006 configuration (222.4 arcsec). Therefore, we adapt a pointing offset of 225 arcsec along the y axis for all footprints in the three spectral bands. The absolute pointing offsets along the footprint axis are summarized in Table 1.

Figure 6 shows the standard deviation of dP_{ABP} and $X_{CO_2,met}$ as a function of the z axis pointing offsets for FP 4 for the Death Valley National Park (for a pointing offset of 225 arcsec along the footprint axis). The analyzed metrics are strongly sensitive to changes of the pointing offset along this axis. We perform a quadratic regression to determine the best estimate of the location of the minimum. We only take data points into account that are distributed symmetrically around the minimum. For FP 4, our analysis indicates a minimum at −124 arcsec for the O_2 A band, −71 arcsec for the weak CO_2 band, and −44 arcsec for the strong CO_2 band. We derive pointing offsets for all other footprints for all three bands in the same way. Figure 7a summarizes the z axis pointing offsets for all footprints for all three bands for the Death Valley National Park and Atacama Desert. On average, the derived pointing offsets for the two areas differ by 13 arcsec for the weak CO_2 band and by 25 arcsec for the strong CO_2 band. For the O_2 A band the differences between the two areas differ, on average, by 46 arcsec. Footprints 3 to 5 have the largest pointing offset values. This is in agreement with the relative footprint geolocations in the v0006 configuration. We average the derived pointing offsets for the CO_2 bands from both hemispheres. This provides the best estimate for the footprint geolocations globally and takes into account that the z axis is rotated by nearly 180° (in glint and nadir mode) when the observatory overpasses the Equator. However, for the O_2 A band, the difference between the pointing offsets for both areas reaches up to 60 arcsec for FP 2. In addition, the Atacama Desert analysis indicate larger relative pointing variations for neighboring footprints. Therefore, for the O_2 A band, we only take the derived pointing offsets from the Death Valley National Park analysis into account. Final pointing offsets for all three bands are derived by applying a quadratic regression to the pointing offsets as a function of footprint. This preserves the parabolic shape of the relative footprint positions, which is supported by findings from the

pre-launch and IOC lunar analysis. The updated pointing offsets for the z axis for each spectral band are summarized in Table 1.

To evaluate the impact of the updated footprint geolocations we sample the surface pressure from GEOS5-FP-IT with the updated meteorological sampling algorithm (that was corrected for the time sampling error) at the footprint geolocations of the O_2 A band. The surface pressure is mainly retrieved from the O_2 A band; therefore sampling the meteorological reanalysis at the O_2 footprint geolocation should yield the best surface pressure estimates. Figure 8 shows the prior surface pressure difference between v8 and sampled at the updated footprint geolocations. The striping pattern effect is mainly introduced by the updated sampling algorithm and follows orbital paths. As stated previously, the updated sampling method also introduces a mean bias of +0.5 hPa between the v8 and newly derived surface pressure estimates. Figure 9 shows the change between the standard deviation of the prior surface pressure in each grid box for both sampling methods. The observed structures are mainly driven by changes in the footprint geolocations. The largest changes are over mountainous regions, e.g., the Tibetan Plateau, the Andes, or the US West Coast. This will mostly manifest as local-scale changes in X_{CO_2}. As expected, there are no significant changes over ocean due to the updated footprint geolocations.

4 The OCO-2 v9 data product

Our improved knowledge of OCO-2's footprint geolocations and the update of the meteorological sampling algorithm reduce errors in bias-corrected X_{CO_2} that were introduced through erroneous surface pressure estimates in the v8 bias correction. The OCO-2 v9 data product combines the v8 ACOS L2FP retrieval results with a revised bias correction using updated surface pressure estimates from GEOS5-FP-IT. Moreover, filter limits that define the X_{CO_2} quality flag and warning levels are adjusted, leading to a larger number of soundings that pass the filtration. Finally, the global scaling factor that is derived from direct observations over TCCON stations is updated. This section highlights the major changes
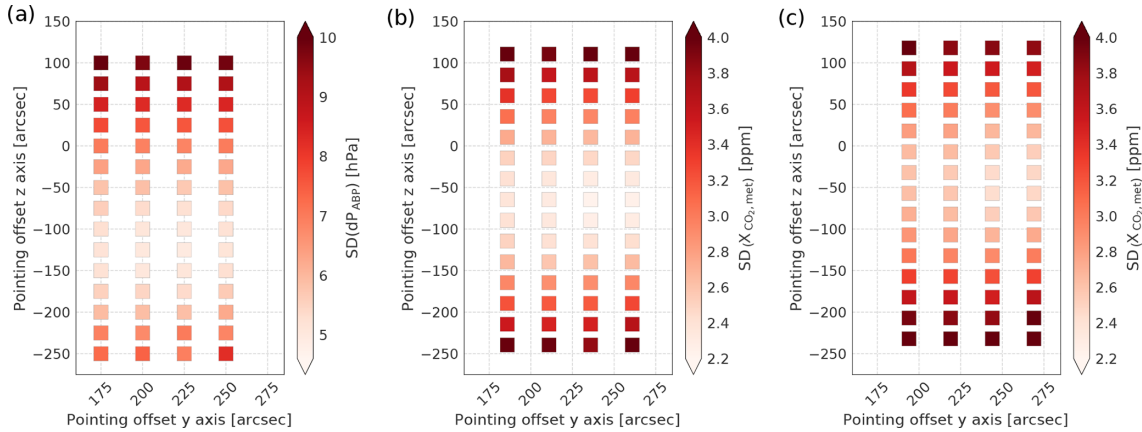
Figure 5. Standard deviation of dP_{ABP} (**a**) and $X_{CO_2,met}$ for the weak (**b**) and strong (**c**) CO_2 band for FP4 for all 60 geolocation configurations for the Death Valley National Park.
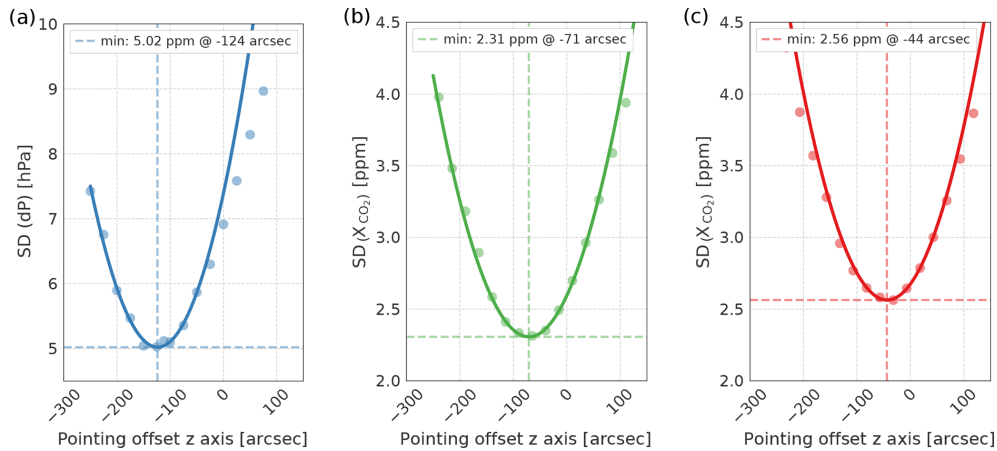

Figure 6. Standard deviation of dP_{ABP} (**a**) and $X_{CO_2,met}$ of the weak (**b**) and strong (**c**) CO_2 bands as a function of z axis pointing offsets for FP4 for the Death Valley National Park. To determine the minimum, only values that are distributed symmetrically around the minimum are taken into account for the quadratic regression.

in OCO-2's v9 X_{CO_2}. The techniques that are used in the next sections are those presented in O'Dell et al. (2018). The derived results, with exception of the revised parametric bias correction, represent updates of the findings in O'Dell et al. (2018).

4.1   Parametric bias correction

The parametric bias correction accounts for spurious variability in X_{CO_2} that is correlated with parameters in the retrieval state vector (Wunch et al., 2017b; O'Dell et al., 2018). A multivariate regression is performed between spurious X_{CO_2} variations and the parameters that account for the largest fraction of the spurious variability. For all ACOS versions for GOSAT and OCO-2 observations, the mode-dependent parametric bias $(X_{CO_2,para})$ has the following form:

$$X_{CO_2,para} = \sum_i c_i \left(p_i - p_{i,ref} \right). \tag{1}$$

Here, c_i are regression coefficients which express the sensitivity of X_{CO_2} from the L2FP retrieval $(X_{CO_2,raw})$ to the selected parameter p_i, and $p_{i,ref}$ are the corresponding reference values. In order to obtain bias-corrected X_{CO_2} $(X_{CO_2,bc})$, Eq. (1) is subtracted from the raw X_{CO_2} retrieved by the L2FP algorithm:

$$\begin{aligned} X_{CO_2,bc} &= X_{CO_2,raw} - X_{CO_2,para} \\ &= X_{CO_2,raw} - \sum_i c_i \left(p_i - p_{i,ref} \right). \end{aligned} \tag{2}$$

Note that we only focus on the parametric bias correction here and neglect the footprint-dependent bias correction and global scaling factor for now. To select the param-

Table 2. Overview of the truth proxy training data sets for v9.

Name	N_s land $\left(\times 10^3\right)$	N_s ocean glint $\left(\times 10^3\right)$	Date	Details
TCCON	614	360	Sep. 2014–May 2018	GGG2014 (see Table 6)
Multi-model median	956	2691	Sep. 2014–March 2017	Median of nine models
SAA	63	287	Sep. 2014–Jan. 2017	Areas < 100 km along-track

Table 3. Models that contribute to the multi-model median truth proxy data set.

| Name/group	Version	Land/biosphere	Inverse method	Transport	Reference
CAMS	15r2	ORCHIDEE	4D-Var	LMDZ	Chevallier et al. (2010)
CarbonTracker	CT2015,CT-NRT.v2016-1	CASA	EnKF	TM5	Peters et al. (2007)
TM5-4DVar-NOAA	2016	SiB-CASA	4D-Var	TM5	Basu et al. (2013)
OU	2016	CASA	4D-Var	TM5	Crowell et al. (2018)
Baker		CASA-GFEDv3	4D-Var	PCTM	Baker et al. (2010)
CMS-Flux		CASA-GFEDv3	4D-Var	GEOS-CHEM	Liu et al. (2017)
CSU-1		SiB4/MERRA	Bayesian Synthesis	GEOS-CHEM	
Jena CarboScope	s04_v3.8	Special	4D-Var	TM3	Rödenbeck (2005)
Univ. Edinburgh	v2.1	CASA	EnKF	GEOS-CHEM	Feng et al. (2009)
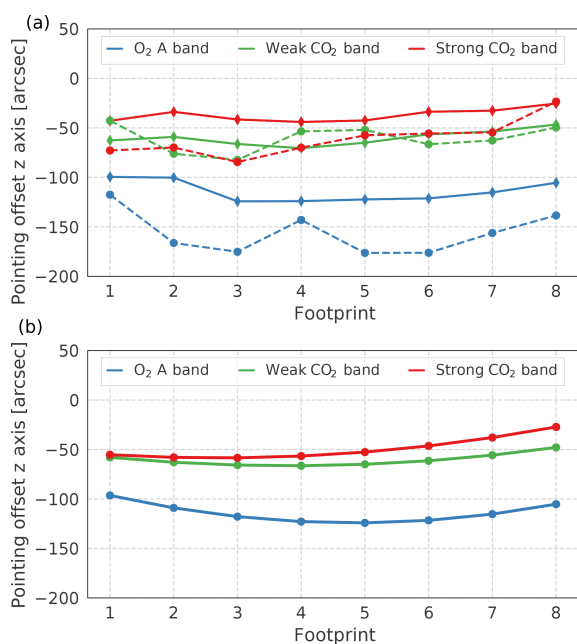
Figure 7. (a) z axis footprint pointing offsets for the three spectral bands for the Death Valley National Park (solid) and Atacama Desert (dashed) and (b) z axis footprint pointing offsets used in the OCO-2 v9 geometric calibration algorithm.

Figure 8. Mean difference between v9 and v8 (v9–v8) surface pressure prior for April 2016. Data are aggregated into $2° \times 2°$ latitude–longitude square grids.

eters and derive the regression coefficients in Eq. (1), different truth proxy training data sets were used for v8: TCCON, small area analysis (SAA), and multi-model median. These truth proxies represent an independent estimate of X_{CO_2} to which we compare OCO-2 X_{CO_2}. A detailed description of the truth proxies is given in Sect. 4.1 in O'Dell
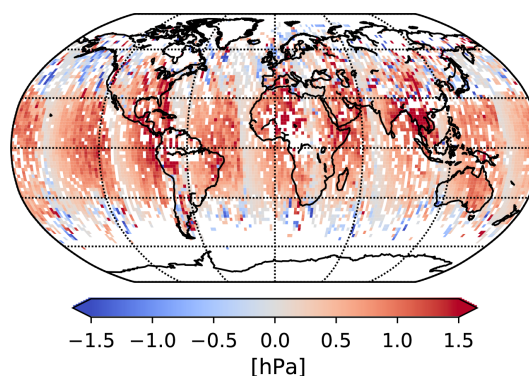
et al. (2018). For v8 land observations, three different parameters were identified that account for the largest fraction of variability: co2_grad_del, DWS, and dP. Over ocean, only co2_grad_del and dP contribute to the parametric bias correction. co2_grad_del represents the tropospheric lapse rate of the retrieved CO_2 profile and is defined as the difference in the retrieved CO_2 between the surface and the retrieval pressure level at 0.6 times the surface pressure, minus the same quantity for the prior profile. DWS represents the combined retrieved optical depth of large particles in the lower-to-middle troposphere in the retrieval, namely dust, water cloud, and sea salt aerosol. In v8, dP is defined as the difference between the retrieved surface pressure and the prior surface pressure from GEOS5-FP-IT.

Table 4. Parametric bias correction coefficients and reference values for v9 over land and ocean.

Land nadir/glint	dP_{frac}	co2_grad_del	DWS
coefficients	-0.900	-0.029	$-9.000\,\mathrm{ppm}$
reference values	$0.0\,\mathrm{ppm}$	$15.0\,\mathrm{ppm}$	0.0
Ocean glint	$dP_{s\mathrm{CO}_2}$	max(co2_grad_del, -6)	
coefficients	$-0.245\,\mathrm{ppm\,hPa}^{-1}$	0.090	
reference values	$0.0\,\mathrm{hPa}$	$-6.0\,\mathrm{ppm}$	
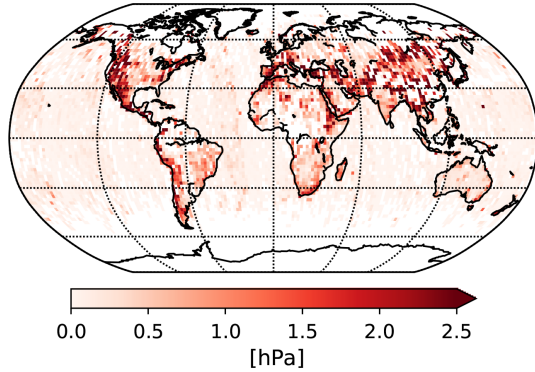
Figure 9. Difference between v9 and v8 (v9–v8) of the surface pressure prior standard deviation in each grid cell for April 2016. Data are aggregated into $2° \times 2°$ latitude–longitude square grids.

For v9, we define two different dP parameters for observations over land (dP_{frac}) and ocean ($dP_{s\mathrm{CO}_2}$) that are used in the parametric bias correction. The revised dP parameters take into account two problems: (1) the misspecifications in the geolocation calibration algorithm for the overall pointing of the observatory and (2) the pointing offsets between the three spectral bands. The first is characterized by the difference between the retrieved surface pressure of the v8 L2FP algorithm ($P_{\mathrm{ret,v8}}$) and the prior surface pressure at the new geolocation where the O_2 A band is pointing (P_{ap,O_2}). The second is characterized by the difference between the prior surface pressure where the O_2 A band is pointing and the prior surface pressure where the strong CO_2 band is pointing ($P_{\mathrm{ap},s\mathrm{CO}_2}$). For ocean, the revised dP parameter has the following form (given in hPa):

$$dP_{s\mathrm{CO}_2} = \left(P_{\mathrm{ret,v8}} - P_{\mathrm{ap},O_2}\right) + \left(P_{\mathrm{ap},O_2} - P_{\mathrm{ap},\mathrm{CO}_2}\right)$$
$$= P_{\mathrm{ret,v8}} - P_{\mathrm{ap},s\mathrm{CO}_2}. \quad (3)$$

This approach allows us to reduce variations in X_{CO_2} due to differences between the retrieved and estimated surface pressure without rerunning the L2FP algorithm. Only the prior surface pressure sampled at the geolocation where the CO_2 bands are pointing is needed. Tests have shown that the best results are achieved when the prior surface pressure is sampled at the geolocation of the strong CO_2 band. Over land, the revised dP parameter accounts for the fractional change

in X_{CO_2} when error is present in surface pressure estimates (given in ppm):

$$dP_{\mathrm{frac}} = X_{\mathrm{CO}_2,\mathrm{raw}} \left(1 - \frac{P_{\mathrm{ap},s\mathrm{CO}_2}}{P_{\mathrm{ret,v8}}}\right). \quad (4)$$

Here, $X_{\mathrm{CO}_2,\mathrm{raw}}$ represents the v8 X_{CO_2} from the L2FP run when no bias correction is applied. A theoretical motivation for our choice of the dP parameters over land and ocean is given in Appendix A. The definitions of co2_grad_del and DWS remains the same in v9.

Similar to v8, we use three truth proxies to derive the parametric bias correction coefficients for co_grad_del, DWS and the revised dP parameters (see Table 2). Compared to v8, the truth proxy data sets are extended in time to cover the longer OCO-2 data record. For the multi-model median, nine models from the OCO-2 model intercomparison project (MIP) are used (see Table 3). For all data sets a correction was applied using the OCO-2 averaging kernels based on Connor et al. (2008). We convolve the CO_2 profiles from the truth proxies with the OCO-2 column averaging kernel before we compare it to OCO-2 X_{CO_2}. The parametric bias correction coefficients for v9 are derived from the average of all coefficients derived from the different truth proxies. The adapted coefficients and reference values for land and ocean glint data are summarized in Table 4. The dP_{frac} coefficient over land is -0.9. This is in agreement with the theoretical value since a change in surface pressure by $\sim 1\%$ also changes X_{CO_2} by $\sim 1\%$ and seems to indicate that the retrieved surface pressure is still not sufficiently accurate to yield the best estimate of X_{CO_2}; indeed, as shown in X_{CO_2}, the coefficient implies that the optimal surface pressure is a weighted average of the retrieved and prior surface pressure, with the prior surface pressure weight being about 0.9. Figure 10 shows the different contributions of the v9 parametric bias correction to the raw X_{CO_2}.

4.2 Quality filters

Bad soundings (e.g., those affected by clouds and low continuum level signal-to-noise ratio) are mostly screened out by the ABP and IDP before the ACOS L2FP algorithm performs retrievals. Some soundings that pass the prescreening criteria, however, show errors in raw X_{CO_2} when compared to the truth proxy training data sets that are too large to provide re-

Table 5. Filter variables and limits for the X_{CO_2} quality flag definition in v9.

Variable	Meaning	Land filter	Ocean filter
co2_ratio	Ratio of Band 2 to Band 3 CO_2 column from IDP algorithm	[1.00, 1.023]	[1.00, 1.02]
h2o_ratio	Ratio of Band 2 to Band 3 H_2O column from IDP algorithm	[0.88, 1.01]	[0.88, 1.01]
dP_{O_2}	Retrieved minus prior surface pressure at geoloc. of O_2 A band (hPa)	[−8, 11]	[−5, 9]
dP_{sCO_2}	Retrieved minus prior surface pressure at geoloc. of strong CO_2 band (hPa)	[−10, 12]	[−5, 9]
dP_{ABP}	Retrieved minus prior surface pressure from ABP algorithm (hPa)	[−12, 16]	[−50, 10]
wind speed	Retrieved surface wind speed ($m\,s^{-1}$)		[1.5, 25]
co2_grad_del	Retrieved vertical gradient in CO_2 (ppm)	[−60, 85]	[−18, 30]
Altitude Stddev	Standard deviation of the surface elevation in the FOV (m)	[0, 110]	
Band 3 albedo	Retrieved albedo strong CO_2 band	[0.03, 0.6]	
albedo_slope_wco2	Retrieved slope of the Lambertian component of the surface albedo using the weak CO_2 band $\left[cm^{-1}\right]$		$[−1.5, 1.2] \times 10^{-5}$
albedo_slope_sco2	Retrieved slope of the Lambertian component of the surface albedo using the strong CO_2 band $\left[cm^{-1}\right]$	$[−13, 100\,] \times 10^{-5}$	$[0.6, 7] \times 10^{-5}$
rms_rel_wco2	Relative rms of Band 2 fit residuals (%)	[0, 0.28]	[0, 0.3]
rms_rel_sco2	Relative rms of Band 3 fit residuals (%)	[0, 0.45]	
τ_{total}	Retrieved optical depth of all aerosol types	[0, 0.5]	
τ_{WA}	Retrieved optical depth of water cloud	[0.0005, 0.1]	
τ_{IC}	Retrieved optical depth of ice cloud	[0.00, 0.04]	[0, 0.035]
τ_{ST}	Retrieved optical depth of stratospheric aerosol	[0.0002, 0.02]	
τ_{OC}	Retrieved optical depth of organic carbon	[0, 0.2]	
τ_{SS}	Retrieved optical depth of sea salt	[0, 0.125]	
H_{IC}	Retrieved relative pressure height of ice cloud	[−0.5, 0.5]	
DWS	Retrieved optical depth of three large aerosol types (dust, water cloud, and sea salt)	[0, 0.25]	
eof33rel	Retrieved relative amplitude of third empirical orthogonal function (EOF) of Band 3		[−0.3, 0.25]
$\chi^2_{wCO_2}$	Reduced χ^2 value of the L2FP fit residuals for Band 2		[0, 2]
$X_{CO_2,uncert.}$	Posterior uncertainty in X_{CO_2} (ppm)		[0.28, 1.10]
Max_Declocking_wco2	See O'Dell et al. (2018) for details		[0, 0.27]
Max_Declocking_sco2	See O'Dell et al. (2018) for details		[0, 0.34]

Table 6. Stations used in the TCCON truth proxy data set.

| TCCON station	Reference	TCCON station	Reference
Anmyeondo, South Korea	Goo et al. (2014)	Lamont, OK, USA	Wennberg et al. (2016)
Ascension Island	Feist et al. (2014)	Lauder, New Zealand	Sherlock et al. (2014)
Białystok, Poland	Deutscher et al. (2014)	Manaus, Brazil	Dubey et al. (2014)
Burgos, Philippines	Velazco et al. (2017)	Ny-Ålesund, Svalbard, Norway	Notholt et al. (2017)
Bremen, Germany	Notholt et al. (2014)	Orléans, France	Warneke et al. (2014)
Caltech, Pasadena, CA, USA	Wennberg et al. (2014b)	Paris, France	Te et al. (2014)
Darwin, Australia	Griffith et al. (2014a)	Park Falls, WI, USA	Wennberg et al. (2014a)
Edwards (Armstrong), CA, USA	Iraci et al. (2016)	Réunion Island	De Mazière et al. (2014)
East Trout Lake, Canada	Wunch et al. (2017a)	Rikubetsu, Japan	Morino et al. (2014b)
Eureka, Canada	Strong et al. (2017)	Saga, Japan	Kawakami et al. (2014)
Garmisch, Germany	Sussmann and Rettinger (2014)	Sodankylä, Finland	Kivi et al. (2014)
Izaña, Tenerife, Spain	Blumenstock et al. (2014)	Tsukuba, Japan	Morino et al. (2014a)
Karlsruhe, Germany	Hase et al. (2014)	Wollongong, Australia	Griffith et al. (2014b)

(a)

(b)

(c)
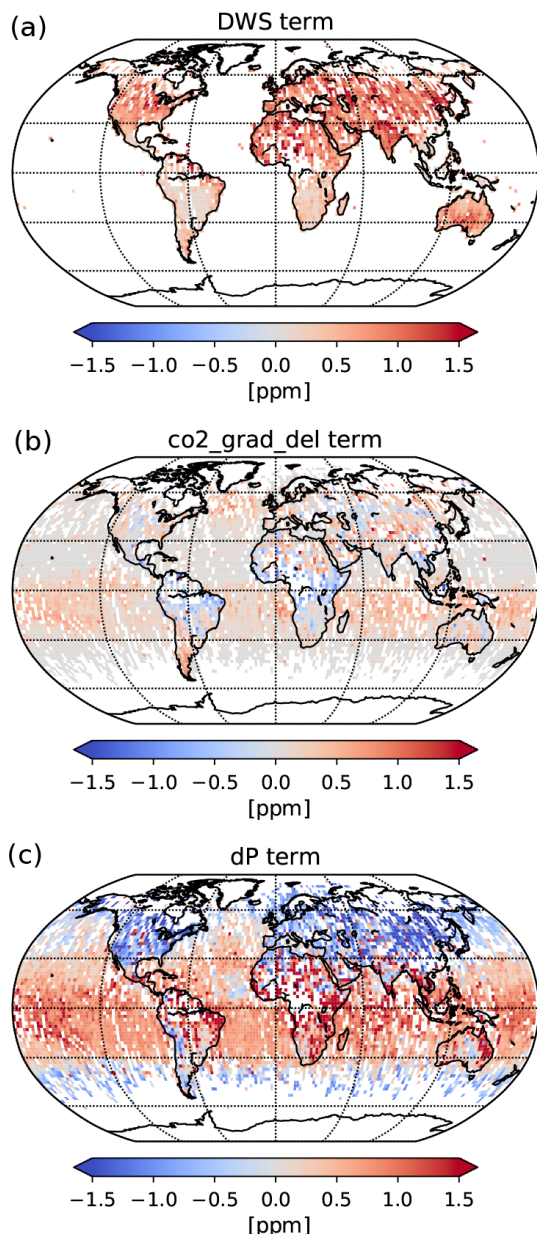
Figure 10. Contributions of the parametric bias correction terms to raw X_{CO_2} from DWS (**a**, only over land), co2_grad_del (**b**), and the two dP terms over land and ocean (**c**) for April 2016. Data are aggregated into $2° \times 2°$ latitude–longitude square grids.

liable constraints on CO_2 fluxes. Therefore, threshold limits are defined for several variables to filter out these soundings. A detailed description on quality filtering is given in Mandrake et al. (2015), Eldering et al. (2017), and O'Dell et al. (2018). We apply slight changes to the v9 filtration.

We introduce the new filter variables dP_{O_2} and dP_{sCO_2}, the difference between the retrieved surface pressure, and the estimated surface pressure at the geolocations of the O_2 A band and dP_{sCO_2} as given in Eq. (3). These variables replace the dP filter variable in v8, which was defined as
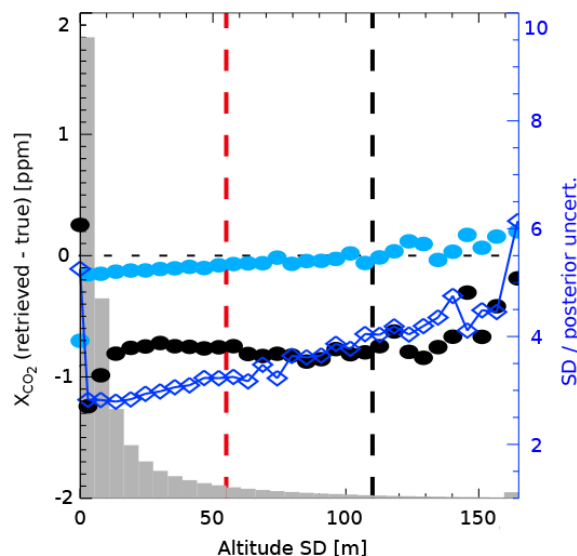
Figure 11. Difference between v9 X_{CO_2} and the multi-model median data set over land (nadir and glint) as a function of the standard deviation of the surface elevation in the FOV given in m. The mean bias, aggregated into 10 m bins, is shown for both raw (black circles) and bias-corrected (light blue circles) X_{CO_2} (corresponding y axis on the left). The standard deviation of the bias-corrected X_{CO_2} difference is marked by dark blue diamonds (corresponding y axis on the right). The distribution of the standard deviation of the surface elevation for the time period September 2014–March 2017 is shown in gray. The vertical dashed black line represents the v9 upper filter limit. The vertical red line represents the upper limit used in v8.
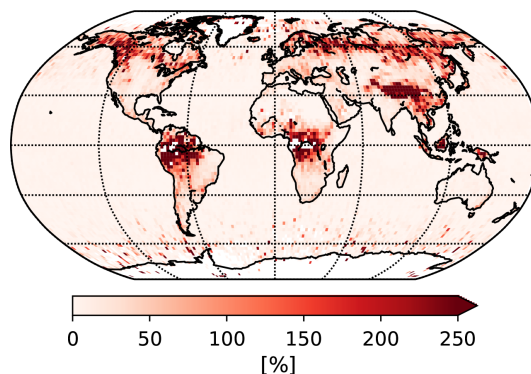

Figure 12. Relative increase of soundings that pass the v9 filtration scheme compared to v8 for the entire year 2016. Data are aggregated into $2° \times 2°$ latitude–longitude square grids.

the difference between the retrieved surface pressure and a mean surface pressure estimate at the geolocation of all three spectral bands. The improved knowledge of the estimated surface pressure values allows us to relax the filter limits for the standard deviation of the surface elevation in the FOV. Figure 9 shows the bias and scatter in X_{CO_2} over land relative to the multi-model median truth proxy data set

as a function of the standard deviation of the surface eleva-
tion. In v9, the scatter in the X_{CO_2} difference starts to in-
crease for standard deviations of the surface elevation larger
than 110 m, whereas in v8 the scatter already increases for
standard deviations larger than 60 m. Therefore, we extend
the rather strict upper filter limit of 60 m in v8 to 110 m.
This leads to a larger throughput of soundings in mountain-
ous areas in v9. The parameters Max_Declocking_wco2 and
Max_Declocking_sco2 are removed from the v9 filtration
scheme over land. Moreover, filter limits for several other
variables changed, e.g., rms_rel_wco2, τ_{oc}, Band 3 albedo,
and dP_{ABP}. The revised filter limits for rms_rel_wco2, τ_{oc},
and Band 3 albedo cause a larger throughput for regions with
boreal forests at high northern latitudes. The updated limits
for τ_{oc} and Band 3 albedo also increase the number of sound-
ings over rain forests. The updated filter limits for dP_{ABP}
cause a larger throughput in regions with bright surfaces, e.g.,
the Saharan desert (see Fig. 12). Overall, 10–15 % additional
soundings pass the new filtration scheme compared to v8. All
v9 filter variables and limits for land and ocean observations
are summarized in Table 5. For soundings that pass filtration
in both v8 and v9, the quality flag did not change.

4.3   Global scaling factor

The global scaling factor corrects for an overall bias in X_{CO_2}
which still remains after filtration and application of the para-
metric bias correction. The global scaling factor is derived by
comparing the OCO-2 data to TCCON measurements which
are tied to the WMO scale (e.g., Wunch et al., 2010; Messer-
schmidt et al., 2010; Geibel et al., 2012). Due to changes in
the data filtration and the revised parametric bias correction
in v9, the global scaling factor C_0 needs to be updated, too.
TCCON stations that are used to derive the global scaling
factor are listed in Table 6.

We use the same geographic and temporal co-location cri-
teria for OCO-2 data from direct overpasses of TCCON sta-
tions as in O'Dell et al. (2018). We apply the OCO-2 av-
eraging kernels to TCCON data as discussed in the deriva-
tion of the coefficients in the parametric bias correction. The
slope of the best fit line (forced through a zero intercept) is
calculated using the method described in York et al. (2004).
The global scaling factor is roughly the same for the differ-
ent observational modes over land and ocean. Ultimately, we
adapt a value of 0.9954 over land and 0.9953 over ocean in
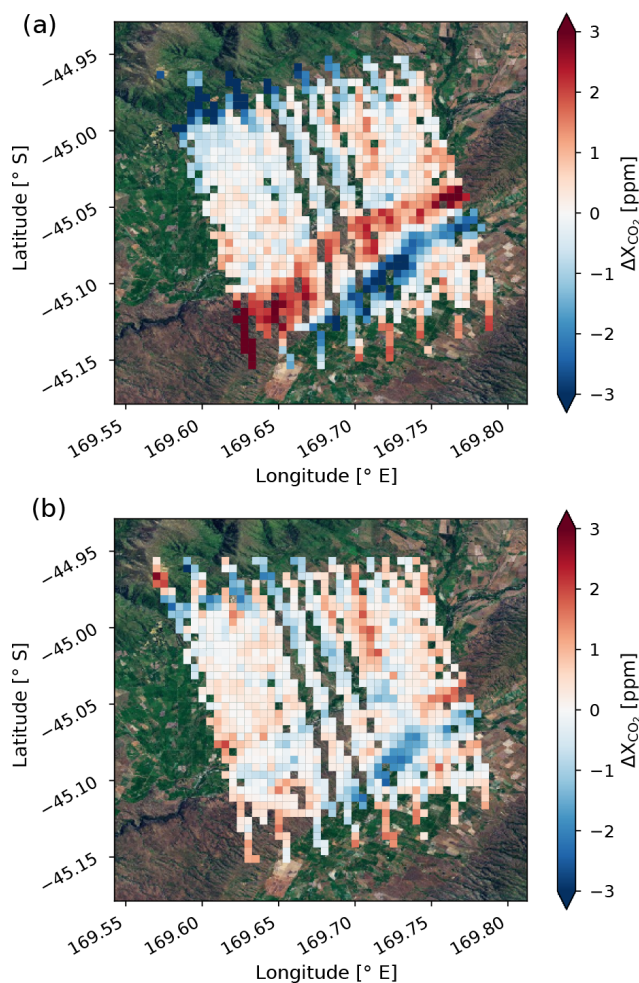v9 (compared with 0.9958 over land and 0.9955 over ocean
in v8).

Figure 13. v8 **(a)** and v9 **(b)** bias-corrected X_{CO_2} over Lauder,
New Zealand, on 17 February 2015. ΔX_{CO_2} is defined in the same
way as in Fig. 1. Data are aggregated into $0.005° \times 0.005°$ latitude–
longitude square grids.

5   Brief evaluation of OCO-2 X_{CO_2} data

Here, we evaluate the impact of the changes made in v9 on
bias-corrected X_{CO_2}. To explore changes on local scales, we
revisit the target observation over Lauder, New Zealand, on
17 February 2015. Figure 13 shows both v8 and v9 bias-
corrected X_{CO_2}. The improved knowledge of the prior sur-
face pressure with the revised parametric bias correction
clearly reduces the correlation between X_{CO_2} and the un-
derlying topography in v9. X_{CO_2} values are distributed more
uniformly over the observed scene. The standard deviation
is reduced from 1.35 ppm in v8 to 0.74 ppm in v9. A small
topography-related bias is still apparent. However, compared
to v8, it is a factor of 2 improvement in reducing biases
caused by erroneous surface pressure estimates.

Figure 14 shows the absolute change in bias-corrected
X_{CO_2} between v8 and v9 globally. The observed changes
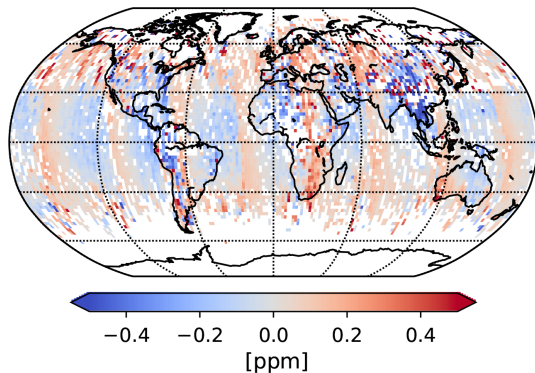are mainly driven by three factors: the updated meteorolog-

Figure 14. Global difference between v8 and v9 (v9–v8) bias-corrected X_{CO_2} for April 2016. Only soundings that passed the v8 and v9 filtration are taken into account. A mean bias of 0.15 ppm (mainly introduced by the different global scaling factors for v8 and v9) is subtracted. Data are aggregated into $2° \times 2°$ latitude–longitude square grids.

ical sampling algorithm, improved knowledge of the footprint geolocations, and the revised parametric bias correction. In analogy to Fig. 8, the striping patterns follow orbital paths and are caused by the updated meteorological sampling algorithm. Differences over mountainous regions like the Tibetan Plateau or the Andes are driven by the improved knowledge of the prior surface pressure due to the updated footprint geolocations. The revised dP_{frac} parameter in the parametric bias correction over land also introduces changes in regions at high altitudes but not necessarily with highly variable topography (e.g., South Africa). In addition, the v9 global scaling factor introduces a systematic difference of approximately +0.15 ppm between v8 and v9.

6 Conclusions

The update of the pointing vector that is used to derive the geolocation for OCO-2's eight footprints, together with an update of the meteorological sampling algorithm that corrects for a temporal sampling coding error, provides a better estimate for the surface pressure in OCO-2's v9 data product. Biases in X_{CO_2} due to erroneous surface pressure estimates are clearly reduced in regions with rough topography. For example, over Lauder, New Zealand, the standard deviation of bias-corrected X_{CO_2} is reduced by almost a factor of 2 when the updated surface pressure estimates are used in the revised parametric bias correction that accounts for misspecifications in the instrument pointing offsets.

Accurate knowledge of the surface pressure and its estimate is crucial to retrieve X_{CO_2} accurately, and many challenges remain. The OCO-2 retrieval, for example, still has a latitudinally dependent bias in surface pressure, with a maximum in the tropics of nearly 5 hPa (O'Dell et al., 2018). Currently, it is thought that this originates in errors in describing the temperature dependence of the oxygen absorption. Moreover, uncertainties in the underlying elevation map and the question what the source of the scattering is might have an impact on surface pressure estimates. This does not only affect X_{CO_2} retrieved from GOSAT and OCO-2 but may also affect future sensors with similar observational approaches.

Appendix A: Theoretical motivation of dP parameters in the v9 parametric bias correction

Column-averaged dry air mole fractions of CO_2 are defined as the total column of CO_2 (C_{CO_2}) divided by the dry air column (C_{dryair}):

$$X_{CO_2} = \frac{C_{CO_2}}{C_{dryair}}. \tag{A1}$$

C_{dryair} is defined as

$$C_{dryair} = \frac{P}{g_0 \cdot m_{dryair}} - \frac{C_{H_2O} \cdot m_{H_2O}}{m_{dryair}}. \tag{A2}$$

Here, P is the surface pressure, g_0 the gravitational acceleration, C_{H_2O} the total column of water vapor, m_{dryair} the mean molecular weight of dry air, and m_{H_2O} the molecular weight of water vapor. The surface pressure P_{true} can be written as

$$P_{true} = a \cdot P_{ap} + (1-a) \cdot P_{ret}. \tag{A3}$$

P_{ap} and P_{ret} represent the prior and retrieved surface pressure, respectively. The parameter a is the fractional weight given to the prior in the assumed surface pressure. A value of $a = 0$ means that we completely trust the retrieval; $a = 1$ means that we completely trust the prior. Because of retrieval biases, the true surface pressure is generally close to the prior surface pressure, such that $a \approx 0.9$. For a start, we neglect the contribution of the total column of water vapor. Then the dry air column is directly proportional to the surface pressure and we can write

$$X_{CO_2,raw} \propto \frac{C_{CO_2}}{P_{ret}}. \tag{A4}$$

For bias-corrected X_{CO_2} we can write

$$
\begin{aligned}
X_{CO_2,bc} &\propto \frac{C_{CO_2}}{a \cdot P_{ap} + (1-a) \cdot P_{ret}} \\
&= \frac{X_{CO_2,raw} \cdot P_{ret}}{a \cdot P_{ap} + (1-a) \cdot P_{ret}} \\
&= \frac{X_{CO_2,raw}}{a \cdot (P_{ap}/P_{ret}) + (1-a)} \\
&= \frac{X_{CO_2,raw}}{1 - a\left(1 - P_{ap}/P_{ret}\right)}.
\end{aligned}
\tag{A5}
$$

Taylor expansion in $x = a\left(1 - P_{ap}/P_{ret}\right)$ around $x = 0$ leads to

$$X_{CO_2,bc} \propto X_{CO_2,raw} + a \cdot \underbrace{X_{CO_2,raw} \cdot \left(1 - \frac{P_{ap}}{P_{ret}}\right)}_{dP_{frac}}. \tag{A6}$$

The second term in Eq. (A6) is identical to the dP_{frac} parameter that is used in the v9 parametric bias correction over land (see Sect. 4.1). Here, a represents the coefficient for the

dP_{frac} parameter in the parametric bias correction over land. Comparing Eq. (A6) to Eq. (2), if $p_1 = dP_{frac}$, then $c_1 = -a$. Further, if we assume that relative variations in $X_{CO_2,raw}/P_{ret}$ are small compared to relative variations in $(P_{ret} - P_{ap})$, then we can simplify to

$$X_{CO_2,bc} = X_{CO_2,raw} + a \cdot (P_{ret} - P_{ap}). \tag{A7}$$

Over ocean, X_{CO_2} typically varies from 390 to 410 ppm and the surface pressure varies from 995 to 1025 hPa. The relative variations of $X_{CO_2,raw}/P_{ret}$ are therefore on the order of a few tenths of a percent on $X_{CO_2,para}$ (for dP), which itself is of the order of 1 ppm and therefore negligible. The second term of Eq. (A7) has the form of the dP_{sCO_2} parameter as defined in Sect. 4.1. This form, however, does not account for the fractional change in X_{CO_2} at higher elevations when error is present in surface pressure estimates. Therefore, we use Eq. (A6) over land and Eq. (A7) only over ocean. Note that the parametric bias correction coefficient a in Eqs. (A6) and (A7) is different for land and ocean observations (see Table 4).

References

Baker, D. F., Bösch, H., Doney, S. C., O'Brien, D., and Schimel, D. S.: Carbon source/sink information provided by column CO_2 measurements from the Orbiting Carbon Observatory, Atmos. Chem. Phys., 10, 4145–4165, https://doi.org/10.5194/acp-10-4145-2010, 2010.

Basu, S., Guerlet, S., Butz, A., Houweling, S., Hasekamp, O., Aben, I., Krummel, P., Steele, P., Langenfelds, R., Torn, M., Biraud, S., Stephens, B., Andrews, A., and Worthy, D.: Global CO_2 fluxes estimated from GOSAT retrievals of total column CO_2, Atmos. Chem. Phys., 13, 8695–8717, https://doi.org/10.5194/acp-13-8695-2013, 2013.

Benson, M., Pierce, L., and Sarabandi, K.: Estimating boreal forest canopy height and above ground biomass using multi-modal remote sensing; a database driven approach, in: 2016 IEEE International Geoscience and Remote Sensing Symposium (IGARSS), 2498–2501, https://doi.org/10.1109/IGARSS.2016.7729645, 2016.

Blumenstock, T., Hase, F., Schneider, M., Garcia, O. E., and Sepulveda, E.: TCCON data from Izana (ES), Release GGG2014R0, TCCON data archive, hosted by CaltechDATA, https://doi.org/10.14291/tccon.ggg2014.izana01.R0/1149295, 2014.

Butz, A., Guerlet, S., Hasekamp, O., Schepers, D., Galli, A., Aben, I., Frankenberg, C., Hartmann, J.-M., Tran, H., Kuze, A., Keppel-Aleks, G., Toon, G., Wunch, D., Wennberg, P., Deutscher, N., Griffith, D., Macatangay, R., Messerschmidt, J., Notholt, J., and Warneke, T.: Toward accurate CO_2 and CH_4 observations from GOSAT, Geophys. Res. Lett., 38, L14812, https://doi.org/10.1029/2011GL047888, 2011.

Chevallier, F., Ciais, P., Conway, T. J., Aalto, T., Anderson, B. E., Bousquet, P., Brunke, E. G., Ciattaglia, L., Esaki, Y., Fröhlich, M., Gomez, A., Gomez-Pelaez, A. J., Haszpra, L., Krummel, P. B., Langenfelds, R. L., Leuenberger, M., Machida, T., Maignan, F., Matsueda, H., Morguí, J. A., Mukai, H., Nakazawa, T., Peylin, P., Ramonet, M., Rivier, L., Sawa, Y., Schmidt, M., Steele, L. P., Vay, S. A., Vermeulen, A. T., Wofsy, S., and Worthy, D.: CO_2 surface fluxes at grid point scale estimated from a global 21 year reanalysis of atmospheric measurements, J. Geophys. Res.-Atmos., 115, D21307, https://doi.org/10.1029/2010JD013887, 2010.

Cogan, A. J., Boesch, H., Parker, R. J., Feng, L., Palmer, P. I., Blavier, J. L., Deutscher, N. M., Macatangay, R., Notholt, J., Roehl, C., Warneke, T., and Wunch, D.: Atmospheric carbon dioxide retrieved from the Greenhouse gases Observing SATellite (GOSAT): Comparison with ground-based TCCON observations and GEOS-Chem model calculations, J. Geophys. Res.-Atmos., 117, D21301, https://doi.org/10.1029/2012JD018087, 2012.

Connor, B. J., Boesch, H., Toon, G., Sen, B., Miller, C., and Crisp, D.: Orbiting Carbon Observatory: Inverse method and prospective error analysis, J. Geophys. Res.-Atmos., 113, D05305, https://doi.org/10.1029/2006JD008336, 2008.

Crisp, D., Fisher, B. M., O'Dell, C., Frankenberg, C., Basilio, R., Bösch, H., Brown, L. R., Castano, R., Connor, B., Deutscher, N. M., Eldering, A., Griffith, D., Gunson, M., Kuze, A., Mandrake, L., McDuffie, J., Messerschmidt, J., Miller, C. E., Morino, I., Natraj, V., Notholt, J., O'Brien, D. M., Oyafuso, F., Polonsky, I., Robinson, J., Salawitch, R., Sherlock, V., Smyth, M., Suto, H., Taylor, T. E., Thompson, D. R., Wennberg, P. O., Wunch, D., and Yung, Y. L.: The ACOS CO_2 retrieval algorithm – Part II: Global X_{CO_2} data characterization, Atmos. Meas. Tech., 5, 687–707, https://doi.org/10.5194/amt-5-687-2012, 2012.

Crisp, D., Pollock, H. R., Rosenberg, R., Chapsky, L., Lee, R. A. M., Oyafuso, F. A., Frankenberg, C., O'Dell, C. W., Bruegge, C. J., Doran, G. B., Eldering, A., Fisher, B. M., Fu, D., Gunson, M. R., Mandrake, L., Osterman, G. B., Schwandner, F. M., Sun, K., Taylor, T. E., Wennberg, P. O., and Wunch, D.: The on-orbit performance of the Orbiting Carbon Observatory-2 (OCO-2) instrument and its radiometrically calibrated products, Atmos. Meas. Tech., 10, 59–81, https://doi.org/10.5194/amt-10-59-2017, 2017.

Crowell, S. M. R., Randolph Kawa, S., Browell, E. V., Hammerling, D. M., Moore, B., Schaefer, K., and Doney, S. C.: On the Ability of Space-Based Passive and Active Remote Sensing Observations of CO_2 to Detect Flux Perturbations to the Carbon Cycle, J. Geophys. Res.-Atmos., 123, 1460–1477, https://doi.org/10.1002/2017JD027836, 2018.

De Mazière, M., Sha, M. K., Desmet, F., Hermans, C., Scolas, F., Kumps, N., Metzger, J.-M., Duflot, V., and Cammas, J.-P.: TCCON data from Reunion Island (RE), Release GGG2014R0, TCCON data archive, hosted by CaltechDATA, https://doi.org/10.14291/tccon.ggg2014.reunion01.R0/1149288, 2014.

Deutscher, N. M., Notholt, J., Messerschmidt, J., Weinzierl, C., Warneke, T., Petri, C., Grupe, P., and Katrynski, K.: TCCON data from Bialystok (PL), Release GGG2014R1, TCCON data archive, hosted by CaltechDATA, https://doi.org/10.14291/tccon.ggg2014.bialystok01.R1/1183984, 2014.

Dubey, M., Henderson, B., Green, D., Butterfield, Z., Keppel-Aleks, G., Allen, N., Blavier, J.-F., Roehl, C., Wunch, D., and Lindenmaier, R.: TCCON data from Manaus (BR), Release GGG2014R0, TCCON data archive, hosted by CaltechDATA, https://doi.org/10.14291/tccon.ggg2014.manaus01.R0/1149274, 2014.

Eldering, A., O'Dell, C. W., Wennberg, P. O., Crisp, D., Gunson, M. R., Viatte, C., Avis, C., Braverman, A., Castano, R., Chang, A., Chapsky, L., Cheng, C., Connor, B., Dang, L., Doran, G., Fisher, B., Frankenberg, C., Fu, D., Granat, R., Hobbs, J., Lee, R. A. M., Mandrake, L., McDuffie, J., Miller, C. E., Myers, V., Natraj, V., O'Brien, D., Osterman, G. B., Oyafuso, F., Payne, V. H., Pollock, H. R., Polonsky, I., Roehl, C. M., Rosenberg, R., Schwandner, F., Smyth, M., Tang, V., Taylor, T. E., To, C., Wunch, D., and Yoshimizu, J.: The Orbiting Carbon Observatory-2: first 18 months of science data products, Atmos. Meas. Tech., 10, 549–563, https://doi.org/10.5194/amt-10-549-2017, 2017.

Feist, D. G., Arnold, S. G., John, N., and Geibel, M. C.: TCCON data from Ascension Island (SH), Release GGG2014R0, TCCON data archive, hosted by CaltechDATA, https://doi.org/10.14291/tccon.ggg2014.ascension01.R0/1149285, 2014.

Feng, L., Palmer, P. I., Bösch, H., and Dance, S.: Estimating surface CO_2 fluxes from space-borne CO_2 dry air mole fraction observations using an ensemble Kalman Filter, Atmos. Chem. Phys., 9, 2619–2633, https://doi.org/10.5194/acp-9-2619-2009, 2009.

Geibel, M. C., Messerschmidt, J., Gerbig, C., Blumenstock, T., Chen, H., Hase, F., Kolle, O., Lavric, J. V., Notholt, J., Palm, M., Rettinger, M., Schmidt, M., Sussmann, R., Warneke, T., and Feist, D. G.: Calibration of column-averaged CH4 over European TCCON FTS sites with airborne in-situ measurements, Atmos. Chem. Phys., 12, 8763–8775, https://doi.org/10.5194/acp-12-8763-2012, 2012.

Goo, T.-Y., Oh, Y.-S., and Velazco, V. A.: TCCON data from Anmeyondo (KR), Release GGG2014R0, TCCON data archive, hosted by CaltechDATA, https://doi.org/10.14291/tccon.ggg2014.anmeyondo01.R0/1149284, 2014.

Griffith, D. W., Deutscher, N. M., Velazco, V. A., Wennberg, P. O., Yavin, Y., Aleks, G. K., Washenfelder, R. a., Toon, G. C., Blavier, J.-F., Murphy, C., Jones, N., Kettlewell, G., Connor, B. J., Macatangay, R., Roehl, C., Ryczek, M., Glowacki, J., Culgan, T., and Bryant, G.: TCCON data from Darwin (AU), Release GGG2014R0, TCCON data archive, hosted by CaltechDATA, https://doi.org/10.14291/tccon.ggg2014.darwin01.R0/1149290, 2014a.

Griffith, D. W., Velazco, V. A., Deutscher, N. M., Murphy, C., Jones, N., Wilson, S., Macatangay, R., Kettlewell, G., Buchholz, R. R., and Riggenbach, M.: TCCON data from Wollongong (AU), Release GGG2014R0, TCCON data archive, hosted by CaltechDATA, https://doi.org/10.14291/tccon.ggg2014.wollongong01.R0/1149291, 2014b.

Haring, R., Pollock, R., Sutin, B. M., and Crisp, D.: The Orbiting Carbon Observatory instrument optical design, Proc. SPIE, 5523, 562693, https://doi.org/10.1117/12.562693, 2004.

Hase, F., Blumenstock, T., Dohe, S., Gross, J., and Kiel, M.: TCCON data from Karlsruhe (DE), Release GGG2014R1, TCCON data archive, hosted by CaltechDATA, https://doi.org/10.14291/tccon.ggg2014.karlsruhe01.R1/1182416, 2014.

Heymann, J., Reuter, M., Buchwitz, M., Schneising, O., Bovensmann, H., Burrows, J. P., Massart, S., Kaiser, J. W., and Crisp, D.: CO_2 emission of Indonesian fires in 2015 estimated from satellite-derived atmospheric CO_2 concentrations, Geophys. Res. Lett., 44, 1537–1544, https://doi.org/10.1002/2016GL072042, 2017.

Iraci, L. T., Podolske, J., Hillyard, P. W., Roehl, C., Wennberg, P. O., Blavier, J.-F., Allen, N., Wunch, D., Osterman, G. B., and Albertson, R.: TCCON data from Edwards (US), Release GGG2014R1, TCCON data archive, hosted by CaltechDATA, https://doi.org/10.14291/tccon.ggg2014.edwards01.R1/1255068, 2016.

Kawakami, S., Ohyama, H., Arai, K., Okumura, H., Taura, C., Fukamachi, T., and Sakashita, M.: TCCON data from Saga (JP), Release GGG2014R0, TCCON data archive, hosted by CaltechDATA, https://doi.org/10.14291/tccon.ggg2014.saga01.R0/1149283, 2014.

Kivi, R., Heikkinen, P., and Kyrö, E.: TCCON data from Sodankyla (FI), Release GGG2014R0, TCCON data archive, hosted by CaltechDATA, https://doi.org/10.14291/tccon.ggg2014.sodankyla01.R0/1149280, 2014.

Liu, J., W. Bowman, K., S. Schimel, D., C. Parazoo, N., Jiang, Z., Lee, M., Bloom, A., Wunch, D., Frankenberg, C., Sun, Y., O'Dell, C., Gurney, K., Menemenlis, D., Gierach, M., Crisp, D., and Eldering, A.: Contrasting carbon cycle responses of the tropical continents to the 2015–2016 El Niño, Science, 358, eaam5690, https://doi.org/10.1126/science.aam5690, 2017.

Lucchesi, R.: File Specification for GEOS-5 FP-IT (Forward Processing for Instrument Teams), Tech. rep., NASA Goddard Spaceflight Center, Greenbelt, MD, USA, available at: https://ntrs.nasa.gov/archive/nasa/casi.ntrs.nasa.gov/20150001438.pdf (last access: 31 March 2019), 2013.

Mandrake, L., O'Dell, C. W., Wunch, D., Wennberg, P. O., Fisher, B., Osterman, G. B., and Eldering, A.: Orbiting Carbon Observatory-2 (OCO-2) Warn Level, Bias Correction, and Lite File Product Description, Tech. rep., Jet Propulsion Laboratory, California Institute of Technology, Pasadena, CA, available at: http://disc.sci.gsfc.nasa.gov/OCO-2/documentation/oco-2-v7/OCO2_XCO2_Lite_Files_and_Bias_Correction_0915_sm.pdf (last access: 31 March 2019), 2015.

Messerschmidt, J., Macatangay, R., Notholt, J., Petri, C., Warneke, T., and Weinzierl, C.: Side by side measurements of CO_2 by ground-based Fourier transform spectrometry (FTS), Tellus B, 62, 749–758, https://doi.org/10.1111/j.1600-0889.2010.00491.x, 2010.

Morino, I., Matsuzaki, T., and Shishime, A.: TCCON data from Tsukuba (JP), 125HR, Release GGG2014R1, TCCON data archive, hosted by CaltechDATA, https://doi.org/10.14291/tccon.ggg2014.tsukuba02.R1/1241486, 2014a.

Morino, I., Yokozeki, N., Matsuzaki, T., and Horikawa, M.: TCCON data from Rikubetsu (JP), Release GGG2014R1, TCCON data archive, hosted by CaltechDATA, https://doi.org/10.14291/tccon.ggg2014.rikubetsu01.R1/1242265, 2014b.

Nassar, R., Hill, T. G., McLinden, C. A., Wunch, D., Jones, D. B. A., and Crisp, D.: Quantifying CO$_2$ Emissions From Individual Power Plants From Space, Geophys. Res. Lett., 44, 10045–10053, https://doi.org/10.1002/2017GL074702, 2017.

NOAA: National Oceanic and Atmospheric Administration – Where is the highest tide?, available at: https://oceanservice.noaa.gov/facts/highesttide.html, last access: August 2018.

Notholt, J., Petri, C., Warneke, T., Deutscher, N. M., Buschmann, M., Weinzierl, C., Macatangay, R., and Grupe, P.: TCCON data from Bremen (DE), Release GGG2014R0, TCCON data archive, hosted by CaltechDATA, https://doi.org/10.14291/tccon.ggg2014.bremen01.R0/1149275, 2014.

Notholt, J., Warneke, T., Petri, C., Deutscher, N. M., Weinzierl, C., Palm, M., and Buschmann, M.: TCCON data from Ny Ålesund, Spitsbergen (NO), Release GGG2014.R0, TCCON data archive, hosted by CaltechDATA, https://doi.org/10.14291/tccon.ggg2014.nyalesund01.R0/1149278, 2017.

O'Dell, C. W., Connor, B., Bösch, H., O'Brien, D., Frankenberg, C., Castano, R., Christi, M., Eldering, D., Fisher, B., Gunson, M., McDuffie, J., Miller, C. E., Natraj, V., Oyafuso, F., Polonsky, I., Smyth, M., Taylor, T., Toon, G. C., Wennberg, P. O., and Wunch, D.: The ACOS CO$_2$ retrieval algorithm – Part 1: Description and validation against synthetic observations, Atmos. Meas. Tech., 5, 99–121, https://doi.org/10.5194/amt-5-99-2012, 2012.

O'Dell, C. W., Eldering, A., Wennberg, P. O., Crisp, D., Gunson, M. R., Fisher, B., Frankenberg, C., Kiel, M., Lindqvist, H., Mandrake, L., Merrelli, A., Natraj, V., Nelson, R. R., Osterman, G. B., Payne, V. H., Taylor, T. E., Wunch, D., Drouin, B. J., Oyafuso, F., Chang, A., McDuffie, J., Smyth, M., Baker, D. F., Basu, S., Chevallier, F., Crowell, S. M. R., Feng, L., Palmer, P. I., Dubey, M., García, O. E., Griffith, D. W. T., Hase, F., Iraci, L. T., Kivi, R., Morino, I., Notholt, J., Ohyama, H., Petri, C., Roehl, C. M., Sha, M. K., Strong, K., Sussmann, R., Te, Y., Uchino, O., and Velazco, V. A.: Improved retrievals of carbon dioxide from Orbiting Carbon Observatory-2 with the version 8 ACOS algorithm, Atmos. Meas. Tech., 11, 6539–6576, https://doi.org/10.5194/amt-11-6539-2018, 2018.

Peters, W., Jacobson, A. R., Sweeney, C., Andrews, A. E., Conway, T. J., Masarie, K., Miller, J. B., Bruhwiler, L. M. P., Pétron, G., Hirsch, A. I., Worthy, D. E. J., van der Werf, G. R., Randerson, J. T., Wennberg, P. O., Krol, M. C., and Tans, P. P.: An atmospheric perspective on North American carbon dioxide exchange: CarbonTracker, P. Natl. Acad. Sci. USA, 104, 18925–18930, https://doi.org/10.1073/pnas.0708986104, 2007.

Pollard, D. F., Sherlock, V., Robinson, J., Deutscher, N. M., Connor, B., and Shiona, H.: The Total Carbon Column Observing Network site description for Lauder, New Zealand, Earth Syst. Sci. Data, 9, 977–992, https://doi.org/10.5194/essd-9-977-2017, 2017.

Rödenbeck, C.: Estimating CO$_2$ sources and sinks from atmospheric mixing ratio measurements using a global inversion of atmospheric transport, Tech. rep., Max Planck Institute for Biogeochemistry, Jena, Germany, available at: http://www.bgc-jena.mpg.de/CarboScope/s/tech_report6.pdf (last access: 31 March 2019), 2005.

Sherlock, V., Connor, B. J., Robinson, J., Shiona, H., Smale, D., and Pollard, D.: TCCON data from Lauder (NZ), 125HR, Release GGG2014R0, TCCON data archive, hosted by CaltechDATA, https://doi.org/10.14291/tccon.ggg2014.lauder02.R0/1149298, 2014.

Strong, K., Mendonca, J., Weaver, D., Fogal, P., Drummond, J., Batchelor, R., and Lindenmaier, R.: TCCON data from Eureka (CA), Release GGG2014R1, TCCON data archive, hosted by CaltechDATA, https://doi.org/10.14291/tccon.ggg2014.eureka01.R1/1325515, 2017.

Suarez, M. J., Rienecker, M. M., Todling, R., Bacmeister, J., Takacs, L., Liu, H. C., Gu, W., Sienkiewicz, M., Koster, R. D., and Gelaro, R.: The GEOS-5 Data Assimilation System-Documentation of Versions 5.0.1, 5.1.0, and 5.2.0, Tech. rep., NASA Goddard Spaceflight Center, Greenbelt, MD, USA, available at: https://ntrs.nasa.gov/archive/nasa/casi.ntrs.nasa.gov/20120011955.pdf (last access: 31 March 2019), 2008.

Sussmann, R. and Rettinger, M.: TCCON data from Garmisch (DE), Release GGG2014R0, TCCON data archive, hosted by CaltechDATA, https://doi.org/10.14291/tccon.ggg2014.garmisch01.R0/1149299, 2014.

Taylor, T. E., O'Dell, C. W., Frankenberg, C., Partain, P. T., Cronk, H. Q., Savtchenko, A., Nelson, R. R., Rosenthal, E. J., Chang, A. Y., Fisher, B., Osterman, G. B., Pollock, R. H., Crisp, D., Eldering, A., and Gunson, M. R.: Orbiting Carbon Observatory-2 (OCO-2) cloud screening algorithms: validation against collocated MODIS and CALIOP data, Atmos. Meas. Tech., 9, 973–989, https://doi.org/10.5194/amt-9-973-2016, 2016.

Te, Y., Jeseck, P., and Janssen, C.: TCCON data from Paris (FR), Release GGG2014R0, TCCON data archive, hosted by CaltechDATA, https://doi.org/10.14291/tccon.ggg2014.paris01.R0/1149279, 2014.

Velazco, V. A., Morino, I., Uchino, O., Hori, A., Kiel, M., Bukosa, B., Deutscher, N. M., Sakai, T., Nagai, T., Bagtasa, G., Izumi, T., Yoshida, Y., and Griffith, D. W. T.: TCCON Philippines: First Measurement Results, Satellite Data and Model Comparisons in Southeast Asia, Remote Sens.-Basel, 9, 1228, https://doi.org/10.3390/rs9121228, 2017.

Warneke, T., Messerschmidt, J., Notholt, J., Weinzierl, C., Deutscher, N. M., Petri, C., Grupe, P., Vuillemin, C., Truong, F., Schmidt, M., Ramonet, M., and Parmentier, E.: TCCON data from Orléans (FR), Release GGG2014R0, TCCON data archive, hosted by CaltechDATA, https://doi.org/10.14291/tccon.ggg2014.orleans01.R0/1149276, 2014.

Wennberg, P. O., Roehl, C., Wunch, D., Toon, G. C., Blavier, J.-F., Washenfelder, R. a., Keppel-Aleks, G., Allen, N., and Ayers, J.: TCCON data from Park Falls (US), Release GGG2014R0, TCCON data archive, hosted by CaltechDATA, https://doi.org/10.14291/tccon.ggg2014.parkfalls01.R0/1149161, 2014a.

Wennberg, P. O., Wunch, D., Roehl, C., Blavier, J.-F., Toon, G. C., and Allen, N.: TCCON data from Caltech (US), Release GGG2014R1, TCCON data archive, hosted by CaltechDATA, https://doi.org/10.14291/tccon.ggg2014.pasadena01.R1/1182415, 2014b.

Wennberg, P. O., Wunch, D., Roehl, C., Blavier, J.-F., Toon, G. C., Allen, N., Dowell, P., Teske, K., Martin, C., and

Martin, J.: TCCON data from Lamont (US), Release GGG2014R1, TCCON data archive, hosted by CaltechDATA, https://doi.org/10.14291/tccon.ggg2014.lamont01.R1/1255070, 2016.

Wu, L., Hasekamp, O., Hu, H., Landgraf, J., Butz, A., aan de Brugh, J., Aben, I., Pollard, D. F., Griffith, D. W. T., Feist, D. G., Koshelev, D., Hase, F., Toon, G. C., Ohyama, H., Morino, I., Notholt, J., Shiomi, K., Iraci, L., Schneider, M., de Mazière, M., Sussmann, R., Kivi, R., Warneke, T., Goo, T.-Y., and Té, Y.: Carbon dioxide retrieval from OCO-2 satellite observations using the RemoTeC algorithm and validation with TCCON measurements, Atmos. Meas. Tech., 11, 3111–3130, https://doi.org/10.5194/amt-11-3111-2018, 2018.

Wunch, D., Toon, G. C., Wennberg, P. O., Wofsy, S. C., Stephens, B. B., Fischer, M. L., Uchino, O., Abshire, J. B., Bernath, P., Biraud, S. C., Blavier, J.-F. L., Boone, C., Bowman, K. P., Browell, E. V., Campos, T., Connor, B. J., Daube, B. C., Deutscher, N. M., Diao, M., Elkins, J. W., Gerbig, C., Gottlieb, E., Griffith, D. W. T., Hurst, D. F., Jiménez, R., Keppel-Aleks, G., Kort, E. A., Macatangay, R., Machida, T., Matsueda, H., Moore, F., Morino, I., Park, S., Robinson, J., Roehl, C. M., Sawa, Y., Sherlock, V., Sweeney, C., Tanaka, T., and Zondlo, M. A.: Calibration of the Total Carbon Column Observing Network using aircraft profile data, Atmos. Meas. Tech., 3, 1351–1362, https://doi.org/10.5194/amt-3-1351-2010, 2010.

Wunch, D., Toon, G. C., Blavier, J.-F. L., Washenfelder, R. A., Notholt, J., Connor, B. J., Griffith, D. W. T., Sherlock, V., and Wennberg, P. O.: The Total Carbon Column Observing Network, Philos. T. R. Soc. A, 369, 2087–2112, https://doi.org/10.1098/rsta.2010.0240, 2011a.

Wunch, D., Wennberg, P. O., Toon, G. C., Connor, B. J., Fisher, B., Osterman, G. B., Frankenberg, C., Mandrake, L., O'Dell, C., Ahonen, P., Biraud, S. C., Castano, R., Cressie, N., Crisp, D., Deutscher, N. M., Eldering, A., Fisher, M. L., Griffith, D. W. T., Gunson, M., Heikkinen, P., Keppel-Aleks, G., Kyrö, E., Lindenmaier, R., Macatangay, R., Mendonca, J., Messerschmidt, J., Miller, C. E., Morino, I., Notholt, J., Oyafuso, F. A., Rettinger, M., Robinson, J., Roehl, C. M., Salawitch, R. J., Sherlock, V., Strong, K., Sussmann, R., Tanaka, T., Thompson, D. R., Uchino, O., Warneke, T., and Wofsy, S. C.: A method for evaluating bias in global measurements of CO_2 total columns from space, Atmos. Chem. Phys., 11, 12317–12337, https://doi.org/10.5194/acp-11-12317-2011, 2011b.

Wunch, D., Mendonca, J., Colebatch, O., Allen, N., Blavier, J.-F. L., Roche, S., Hedelius, J. K., Neufeld, G., Springett, S., Worthy, D. E. J., Kessler, R., and Strong, K.: TCCON data from East Trout Lake (CA), Release GGG2014R1, TCCON data archive, hosted by CaltechDATA, https://doi.org/10.14291/tccon.ggg2014.easttroutlake01.R1, 2017a.

Wunch, D., Wennberg, P. O., Osterman, G., Fisher, B., Naylor, B., Roehl, C. M., O'Dell, C., Mandrake, L., Viatte, C., Kiel, M., Griffith, D. W. T., Deutscher, N. M., Velazco, V. A., Notholt, J., Warneke, T., Petri, C., De Maziere, M., Sha, M. K., Sussmann, R., Rettinger, M., Pollard, D., Robinson, J., Morino, I., Uchino, O., Hase, F., Blumenstock, T., Feist, D. G., Arnold, S. G., Strong, K., Mendonca, J., Kivi, R., Heikkinen, P., Iraci, L., Podolske, J., Hillyard, P. W., Kawakami, S., Dubey, M. K., Parker, H. A., Sepulveda, E., García, O. E., Te, Y., Jeseck, P., Gunson, M. R., Crisp, D., and Eldering, A.: Comparisons of the Orbiting Carbon Observatory-2 (OCO-2) X_{CO_2} measurements with TCCON, Atmos. Meas. Tech., 10, 2209–2238, https://doi.org/10.5194/amt-10-2209-2017, 2017b.

Yang, Z., Wennberg, P., Cageao, R., Pongetti, T., Toon, G., and Sander, S.: Ground-based photon path measurements from solar absorption spectra of the O_2 A-band, J. Quant. Spectrosc. Ra., 90, 309–321, 2005.

York, D., Evensen, N. M., Martínez, M. L., and De Basabe Delgado, J.: Unified equations for the slope, intercept, and standard errors of the best straight line, Am. J. Phys., 72, 367–375, https://doi.org/10.1119/1.1632486, 2004.